

1 **Nuclear blebs are associated with destabilized chromatin packing**
2 **domains**

3

4 **AUTHOR LIST AND AFFILIATIONS**

5 Emily M. Pujadas Liwag^{1,2,3, +}, Nicolas Acosta^{1,3 +}, Luay Matthew Almassalha^{1,3,4+}, Yuanzhe
6 (Patrick) Su^{1,3}, Ruyi Gong^{1,3}, Masato T. Kanemaki^{5,6,7}, Andrew D. Stephens^{8,9, *}, Vadim
7 Backman^{1,3, *, †}

8

9 ¹ Department of Biomedical Engineering, Northwestern University, Evanston, Illinois, 60208, USA

10 ² IBIS Interdisciplinary Biological Sciences Graduate Program, Northwestern University, Evanston, Illinois, 60208,
11 USA

12 ³ Center for Physical Genomics and Engineering, Northwestern University, Evanston, Illinois, 60208, USA

13 ⁴ Department of Gastroenterology and Hepatology, Northwestern Memorial Hospital, Chicago, IL 60611, USA

14 ⁵ Department of Chromosome Science, National Institute of Genetics, ROIS, Mishima, Shizuoka 411-8540, Japan

15 ⁶ Graduate Institute for Advanced Studies, SOKENDAI, Mishima, Shizuoka 411-8540, Japan

16 ⁷ Department of Biological Science, The University of Tokyo, Tokyo 113-0033, Japan

17 ⁸ Biology Department, University of Massachusetts Amherst, Amherst, MA. 01003

18 ⁹ Molecular and Cellular Biology, University of Massachusetts Amherst, Amherst, MA 01003, USA

19

20

21 ⁺co-first authors (contributed equally) and each has the right to place their name first on
22 curriculum vitae

23

24 *Correspondence: Andrew.stephens@umass.edu (A.D.S.), v-backman@northwestern.edu
25 (V.B.)

26 [†] Lead Contact

27

28

29

30

31

32

33

34

35 **SUMMARY STATEMENT**

36 Nuclear blebs are linked to various pathologies, including cancer and premature aging
37 disorders. We investigate alterations in higher-order chromatin structure within blebs, revealing
38 fragmentation of nanoscopic heterochromatin domains.

39

40 **ABSTRACT**

41 Disrupted nuclear shape is associated with multiple pathological processes including premature
42 aging disorders, cancer-relevant chromosomal rearrangements, and DNA damage. Nuclear
43 blebs (i.e., herniations of the nuclear envelope) have been induced by (1) nuclear compression,
44 (2) nuclear migration (e.g., cancer metastasis), (3) actin contraction, (4) lamin mutation or
45 depletion, and (5) heterochromatin enzyme inhibition. Recent work has shown that chromatin
46 transformation is a hallmark of bleb formation, but the transformation of higher-order structures
47 in blebs is not well understood. As higher-order chromatin has been shown to assemble into
48 nanoscopic packing domains, we investigated if (1) packing domain organization is altered
49 within nuclear blebs and (2) if alteration in packing domain structure contributed to bleb
50 formation. Using Dual-Partial Wave Spectroscopic microscopy, we show that chromatin packing
51 domains within blebs are transformed both by B-type lamin depletion and the inhibition of
52 heterochromatin enzymes compared to the nuclear body. Pairing these results with single-
53 molecule localization microscopy of constitutive heterochromatin, we show fragmentation of
54 nanoscopic heterochromatin domains within bleb domains. Overall, these findings indicate that
55 translocation into blebs results in a fragmented higher-order chromatin structure.

56

57 **INTRODUCTION**

58 The mammalian cell nucleus is a membrane-enclosed organelle that provides an enclosure for
59 chromatin, the assembly of DNA and associated proteins that regulates critical processes such
60 as gene transcription, replication, and DNA repair. Chromatin, chromatin proteins, and
61 chromatin-related processes directly influence nuclear mechanics and shape.[1-5] Nuclear
62 stability is further maintained by multiple processes, including by the nuclear lamina, a
63 meshwork of type V intermediate filament proteins called lamins.[6] Besides its role in
64 maintaining nuclear stiffness and stability, the lamina plays critical roles in regulating gene
65 expression and DNA replication through chromatin interactions.[2] Located immediately
66 underneath the inner nuclear membrane, the lamina consists of four major types of lamin
67 proteins: lamin A, lamin C, lamin B1, and lamin B2. A-type lamins, which consist of lamins A and
68 C, are primarily associated with developmental roles, contribute to nuclear stiffness, mainly
69 expressed in differentiated cells, and are spatially located near the nucleoplasm.[1, 7] B-type

70 lamins, in contrast, are expressed in all cell types throughout development and differentiation,
71 provide global integrity of chromatin structure through chromatin-tethering, and are tightly
72 associated with the inner nuclear membrane.[7-9] In mammalian cells, lamins interact with
73 heterochromatin to form lamina-associated domains (LADs), identified through the DamID
74 technique which maps protein-DNA interactions in a genome-wide manner, and are typically
75 transcriptionally repressive environments.[10-12] Disruption of these LADs has been linked to
76 epigenetic changes in cancer and pre-malignant processes such as the onset and evasion of
77 senescence.[13]

78
79 Abnormal nuclear morphology and disruption of genome organization are associated with
80 pathologies such as laminopathies (e.g., Hutchinson-Gilford progeria syndrome), cancer, and
81 cardiac disorders.[2, 14, 15] Among the most radical transformations in nuclear shape is the
82 protrusion of chromatin from the nuclear surface, known as a nuclear bleb, that are associated
83 with pathological transformation.[2, 6, 15, 16] While these blebs are highly associated with
84 gene-rich euchromatin and are believed to only contain lamin A/C,[7] recent evidence has
85 indicated that non-canonical blebs also contain B-type lamins.[2, 17, 18] A- and B-type lamins
86 both contribute to nuclear mechanics and morphology, and depletion of either has been widely
87 shown to induce both abnormal nuclear shape and a higher propensity for nuclear rupture,
88 increased presence of micronuclei, and more nuclear blebbing events.[14, 16, 19] Nucleus
89 micromanipulation force measurements reveal that the nucleus is softer upon inhibition of either
90 histone deacetylation (HDAC) or histone methyltransferase (HMT) which leads to nuclear bleb
91 formation independent of lamins.[2, 15] Thus, chromatin and lamins resist external antagonistic
92 forces from actin contraction[7, 20-22] and compression[23, 24], as well as internal transcription
93 forces[4], to maintain nuclear shape. These studies indicate that nuclear mechanics are
94 influenced by the balance of euchromatin and heterochromatin, and that perturbation of this
95 balance can result in abnormal nuclear morphology and DNA damage, both hallmarks of human
96 disease.[15, 16, 25] At the nuclear periphery, the dynamics of cytoskeleton reorganization and
97 chromatin structural changes contribute to mechano-transduction and transcription, independent
98 of lamins. For example, mechanosensitive ion channels embedded in the plasma membrane
99 activate Ca^{2+} signaling upon cellular stress, which can contribute to heterochromatin
100 reorganization and chromatin mobility.[15, 26-28]

101
102 Recent work demonstrates that chromatin assembles into higher-order polymeric domain
103 structures (nanodomains, packing domains, cores), which range between 50-200 nm in size

104 and contain ~200 Kbp to 2Mbp of genomic content across multiple cell types.[29-31] A crucial
105 feature of these domains is the formation of high-density centers with surrounding regions of
106 decreased density until a transition into low-density space with RNA-polymerase activity forming
107 primarily at the boundary. In the context of these findings, the structure of the genome
108 assembles from disordered nucleosomes (5 to 25nm) transitioning into domains (50-150nm)
109 and then into territorial polymers (>200nm). As has been previously shown, within the regime of
110 chromatin assembling into domains, chromatin acts as a power-law polymer with dimension, D
111 relating how the mass is distributed within the occupied volume. Notably, within supra-
112 nucleosomal length scales, chromatin is not assembled purely as a space-filling globule ($D=3$)
113 nor is it as a poorly structured polymer with monomers primarily favors solvent interactions
114 ($D=5/3$), instead it is typically within these ranges and varies from cell to cell. A key feature
115 identified in this higher-order assembly is the coupling between heterochromatin centers (dense
116 cores) with euchromatic periphery and a corrugated periphery [30]. As power-law polymeric
117 assemblies, the structure of these chromatin packing domains is quantifiable by the relationship
118 $M \propto r^D$, relating how genome content fills an occupied volume as a function of its radial distance,
119 r . Notably, this organization can be directly measured by live-cell dual-Partial Wave
120 Spectroscopic (dual-PWS) Microscopy and quantified by the fractal dimension, D (**Materials**
121 **and Methods**). In addition to quantifying packing domain structure in live cells, PWS
122 microscopy allows measurement of the effective diffusion coefficient, D_e , and the fractional
123 moving mass (FMM) which quantifies the fraction of chromatin demonstrating coherent motion
124 within a diffraction limited volume. Utilizing this technique, we have previously demonstrated
125 that B-type lamin depletion is associated with increased levels of chromatin fractional moving
126 mass and repositioning of heterochromatin cores [32, 33].

127
128 A major challenge in studying alteration in chromatin due to blebbing is that these represent
129 infrequent, but critical events in nuclear structure. As such, they are difficult to assess using
130 sequencing-based methods that measure ensemble chromatin organization such as Hi-C or
131 ChIP-Seq and require the utilization of microscopic methods that can directly quantify changes
132 in high-order genome structure. Therefore, in this study, we utilize live-cell PWS microscopy to
133 investigate the interplay between the disruption of the nuclear lamina and heterochromatin
134 enzymes in the structure of higher-order chromatin within blebs. Our results indicate distinct
135 roles for the nuclear lamina and heterochromatin remodeling processes in regulating higher-
136 order chromatin domains both of which are associated with bleb formation. Finally, pairing our

137 findings with super-resolution microscopy, we show that a key transformation of higher-order
138 chromatin within blebs is that of nanoscopic cores.

139

140 RESULTS

141 B-type lamin depletion or heterochromatin loss promote aberrant nuclear morphology in 142 HCT-116 cells

143 Bleb formation has been identified in numerous cell types, but the frequencies of bleb formation
144 have been shown to depend on multiple factors. Therefore, we first investigated the role of
145 processes well established to induce bleb formation: inhibition of B-type lamins and disruption in
146 heterochromatin enzymes.[2, 34] To assess the impact of lamin degradation on nuclear
147 morphology, we applied the AID system to HCT116 colorectal carcinoma epithelial cells to
148 induce simultaneous degradation of lamin B1 and lamin B2 as previously described.[32, 33, 35]
149 Using immunofluorescence imaging, we quantified the percentages of nuclear blebbing in
150 HCT116^{LMN(B1&B2)-AID} cells before and after depletion of B-type lamins by auxin treatment for 24
151 hours. We found that in comparison to untreated controls, auxin treatment promoted a
152 significant increase in the percentage of cells containing nuclear blebs (2.07% vs 6.23%; 4.163
153 \pm 1.033 (Mean difference \pm SEM), p-value = 0.016, Student's t-test) (**Fig. 1A; Fig. S1A**), in
154 agreement with past studies. [2, 36, 37] Previous work from this group has demonstrated that
155 inhibition of HDACs to increase euchromatin content in mammalian cells or inhibition of histone
156 methyltransferases to decrease heterochromatin content results in a softer nucleus and
157 promotes nuclear blebbing, without perturbing lamins.[2, 15] We therefore hypothesized that in
158 addition B-type lamin loss increasing nuclear blebbing, heterochromatin loss would also result in
159 a substantial increase in nuclear deformations in HCT-116 cells. To test this, we treated
160 HCT116^{LMN(B1&B2)-AID} cells with either GSK343, an inhibitor of the histone methyltransferase
161 Enhancer of Zeste Homolog 2 (EZH2), or Trichostatin A (TSA), an inhibitor of class I and II
162 HDACs for 24 hours.

163

164 Our results confirmed that GSK343 and TSA treatment significantly increased the percentage of
165 blebbed nuclei within HCT-116 cells; with TSA treatment also inducing micronuclei formation
166 and associated with severely deformed nuclear periphery (**Fig. 1B; Fig. S1A**). The effect of TSA
167 treatment on nuclear blebbing frequency was drastically higher than that of auxin or GSK343 in
168 HCT116^{LMN(B1&B2)-AID} cells (Auxin 6.23%, GSK343 6.99%, TSA 15.32%). Next, we explored how
169 combined treatment of either auxin and GSK343 or auxin and TSA would impact the frequency
170 of nuclear deformations. In contrast to prior work, combination of inhibition of b-type lamins with

171 disruption of heterochromatin resulted in only slightly increased rates of nuclear deformations in
172 comparison to lamin depletion, GSK343, or TSA treatment alone (Auxin + GSK343 7.97%,
173 Auxin + TSA 23.56%) (**Fig. 1C**; **Fig. S1A**). Using immunofluorescence microscopy, we
174 visualized these blebs and compared relative levels of H3K27me3 and H3K27ac between the
175 untreated control and auxin, GSK343, and TSA-treated conditions within the cell nucleus (**Fig.**
176 **1D**). Consistent with prior reports, we observe a reduction in H3K27me3 levels upon auxin-
177 induced degradation of B-type lamins, GSK343, and TSA treatment, however, only a
178 concomitant increase in H3K27ac levels was observed in the auxin-treatment group (**Fig. 1E,**
179 **F**). Taken together, these results indicated that TSA-mediated heterochromatin disruption
180 promotes nuclear deformations to similar levels or greater levels than B-type lamin loss in HCT-
181 116 cells.

182

183 **Nanoscale chromatin packing domains are disrupted within nuclear blebs**

184 We recently demonstrated that the decreased DNA density is conserved across multiple bleb
185 mechanisms and is a consistently preserved feature of blebs. We investigate here in greater
186 detail the influence in the change of higher-order chromatin organization upon bleb formation.
187 We have previously shown that live-cell PWS microscopy, which does not resolve each
188 individual domain but measures the local ensemble in individual nuclei (**Materials and**
189 **Methods**), is sensitive to detecting the assembly into supra-nucleosome structures in individual
190 cells with measurements comparable to those observed on electron microscopy by measuring
191 the variations in the visible-light interference spectrum from within the nucleus. [29, 30, 38-40]
192 Likewise, we have shown that by analyzing the temporal interference spectrum at a single-
193 wavelength dual-PWS microscopy can measure the temporal evolution of chromatin density and
194 the fractional moving mass (FMM), which measures the volume fraction of- and mass of-
195 chromatin moving coherently with a sensitivity to mass density fluctuations as low as $\sim 5 \times 10^{-21}$
196 grams, and the effective diffusion coefficient (D_e) within the nucleus (ranging between
197 $\sim 0.065 \mu\text{M}^2/\text{s}$ to $3.5 \times 10^{-5} \mu\text{M}^2/\text{s}$). In the context that the mass of an individual nucleosome $\sim 10^{-19}$
198 grams, the typical values of FMM measured represent the movement of nucleosome clutches
199 moving coherently (as an ensemble). With respect to the D_e , the observed values are typically
200 between the observed rate of diffusion for genomic loci ($\sim 10^{-4} \mu\text{M}^2/\text{s}$) and the rate of mRNA
201 through the nucleus ($\sim 5 \times 10^{-2} \mu\text{M}^2/\text{s}$). [30] Given these considerations, we utilized dual-live cell
202 PWS microscopy to probe the higher-order structure of chromatin in blebs, nuclei with blebs,
203 and stable nuclei.

204

205 Applying dual-PWS to the three well known processes that contribute to bleb formation, we
206 investigated the structure of higher order chromatin and mobility in B-type lamin depletion,
207 HDAC inhibition, and in EZH2 inhibition. As each perturbation have a distinct means to promote
208 bleb formation, we first evaluated the structure of chromatin packing domains observed within
209 blebs in all conditions (controls, EZH2i, HDACi, and lamin depletion) to see if any commonalities
210 were present (**Table 1; Fig. 2A-F**). Overall, this indicated that independent of the mechanism of
211 bleb formation, relative to the nuclear body higher-order chromatin organization within blebs
212 was associated with a lower-likelihood of well-formed packed domains (low D) and fragmented
213 clutches (decreased FMM) with increased mobility (D_e). Comparing the observed behavior of
214 chromatin domains across the nuclei in these conditions, we observed that treatment with EZH2
215 or TSA resulted in decreased D with an associated increase in FMM in comparison to untreated
216 controls whereas D and FMM increased upon B-type lamin depletion, indicating that disruption
217 of heterochromatin enzymatic processes result in fragmentation of chromatin domains and the
218 loss of coherent chromatin motion. Next, we compared the behavior of chromatin domains
219 within blebs across all conditions and unexpectedly observed that domains associated due to
220 lamin B depletion had a comparably higher D and FMM compared to those that occur due to
221 inhibition of heterochromatin remodeling enzymes (**Fig. 2A, B, D, E; Fig. S1B, C**). As such,
222 these results suggest that the domains translocating into blebs are larger in size and more
223 stable with the disruption of the lamina compared to the other conditions. As removal of B-type
224 lamins led to a significant increase in nuclear blebbing, these findings point to a bleb-associated
225 chromatin phenotype, in which nuclear blebs contain fewer packing domains, and B-type lamin
226 degradation could reduce the barriers for nuclear bleb formation that results from the
227 restructuring or redistribution of packing domains.

228
229 To further characterize the temporal dynamics of nuclear blebbing induced by either B-type
230 lamin loss or heterochromatin disruption, we used dual-PWS to measure chromatin mobility
231 between nuclear bleb and nuclear body in live cells. As TSA treatment resulted in the most
232 substantial increase in the frequency of nuclear deformations above, we treated
233 HCT116^{LMN(B1&B2)-AID} cells with either DMSO or TSA. By measuring the spectral interference at a
234 single wavelength as a function of time from within nuclei and within blebs, we could directly
235 image and measure how mass was transitioning between these phases.[39] As discussed
236 previously, variations in the temporal interference quantifies the FMM while the spatially-
237 average signal is inversely proportional the chromatin volume concentration (chromatin
238 density).[39, 41] Utilizing this approach, we can visualize without labels the temporal evolution

239 of chromatin density in both the nucleus and the bleb with a temporal resolution of 50ms per
240 frame (acquired over 15s total in this instance). On imaging chromatin motion in the DMSO
241 control nuclei, its visually apparent that density moves randomly over these timescales. In
242 contrast, within a TSA treated cell with a visually apparent bleb, chromatin decreases rapidly
243 adjacent to the nuclear bleb (**Fig. 3A, B; Movie S1-3**). Between the nuclear bleb and the main
244 nuclear body in TSA treatment, we observed the active transit of small amounts of mass as
245 evidenced by increased local chromatin density and the visual changing of density in the bleb.
246 Comparing the density of chromatin within DMSO associated and TSA induced blebs, TSA
247 blebs unexpectedly had higher chromatin concentration compared to the DMSO control group
248 (**Fig. 3C**). Our results therefore further suggest that the mobilization of chromatin packing
249 domains is an active process during nuclear blebbing induced by B-type lamin and
250 heterochromatin loss.

251

252 **Super-resolution imaging of chromatin heterochromatin domains in nuclear blebs**

253 Nuclear lamins and heterochromatin have been shown to act in parallel to maintain the
254 mechanical properties of the nucleus but the consequence of these on chromatin nanodomains
255 in bleb formation have not been investigated.[28, 34, 42] Additionally, chromatin structure and
256 dynamics are often closely related, which may support mechanisms of either granting or limiting
257 access to regions with high local chromatin concentration[43]. In the context of prior work
258 suggesting that chromatin domains are composed of high-density, presumably heterochromatic
259 centers[29-31, 44], we investigated the transformation in constitutive heterochromatin domains
260 between the nuclear bleb and the nuclear body in spontaneously forming blebs (controls), in
261 lamin B1/B2 depletion-associated blebs, and in heterochromatin enzyme-inhibited blebs (TSA)
262 using super-resolution microscopy. Due to the limitation of bleb formation being a low-frequency
263 process (< 15% of the time), we were only able to identify blebs in a few nuclei in total in HCT-
264 116 cells (**Fig. 4A-C**). Given this limitation, we utilized a second cell-line model, U2OS cells, that
265 were associated with higher rates of bleb formation upon HDAC inhibition with TSA (**Fig. 4D-E**).

266

267 Visually, we observed distinct differences in H3K9me3 chromatin nanodomains in these three
268 conditions. In blebs formed spontaneously (**Fig. 4A**), blebs formed in B-type lamin depletion
269 (**Fig. 4B**), and blebs formed due to inhibition of histone deacetylases (**Fig. 4C, E**), it is visually
270 apparent that nanoscopic heterochromatin domains are observed. Within the nuclear body, as
271 previously demonstrated[32, 33], auxin-induced depletion of B-type lamins resulted in reduced
272 peripheral heterochromatic cores at the nuclear periphery, however, domains formed within the

273 nuclear interior were typically larger in size (**Fig. S2**). With respect to heterochromatin
274 nanodomains in GSK343 treated HCT116 cells[32, 33] and TSA treated U2OS cells, these were
275 smaller than those in control cells and in lamin B-depletion as expected due to the inhibition of
276 heterochromatin enzymes within the nuclear body (**Fig. 4D-F; Fig. S2**). In contrast to prior work,
277 we found that the nuclear blebs arising from either B-type lamin degradation or TSA treatment
278 contained heterochromatin around the periphery of blebs and within the center of the bleb (**Fig.**
279 **4C, E, F; Fig. S2**). This finding highly contradicts the plethora of research stating that all nuclear
280 blebs are devoid of heterochromatin.[45-47] Instead, these results show that independent B-
281 type lamin loss, HDAC inhibition gives rise to non-canonical nuclear blebs enriched in
282 heterochromatin around near their boundaries and the transfer of nanoscopic heterochromatin
283 domains into the bleb. This also challenges the notion that euchromatin enrichment is the most
284 reliable marker of nuclear blebs[17], and further suggests that other cellular mechanisms could
285 play a role in the morphological properties of these herniations.

286

287 **DISCUSSION**

288 In this work, we found that nuclear packing domains are transformed within blebs induced by
289 the loss of either B-type lamins or inhibition of heterochromatin enzymes. Specifically, the
290 domains observed within blebs were typically poorly formed, with increased fragmentation and a
291 higher effective diffusion coefficient compared to the domains observed in the nuclear body
292 independent of the conditions. Despite the conserved differences across groups, we notably
293 saw that in domains associated with lamin B depletion, these were larger than those produced
294 by inhibition of heterochromatin remodeling enzymes (GSK343 inhibition of EZH2 and TSA
295 inhibition of HDACs) suggesting that the barrier to movement of domains or nucleosome
296 clutches is larger in the loss of b-type lamins whereas the inhibition of heterochromatin enzymes
297 fragments domains to facilitate deformations in the nuclear border (**Fig. 2A, D**). Given these
298 findings, one possible and interesting explanation is that domains or clutches of nucleosomes
299 move in concert into blebs through transiently evolving defects in the nuclear lamina. As such,
300 depletion of b-type lamins may increase the frequency of barrier disruption events or potentially
301 result in larger transient defects that allow passage of larger domains into the bleb body. Further
302 supporting these findings were the observation that the structure of heterochromatin domains
303 upon B-type lamin depletion are larger in size compared to those in nuclei treated with
304 heterochromatin enzyme inhibitors on super-resolution microscopy (**Fig. 4A, B**). Likewise,
305 although limited the low frequency of bleb events, domains observed within all blebs were

306 smaller in size and more disperse than those observed in the adjacent nuclear body (**Fig. 4A,**
307 **B**).

308
309 The changes observed in chromatin domains within blebs could be related to functional
310 consequences in signaling, possibly arising from applied mechanical stress when the nuclear
311 lamina or heterochromatin are disrupted. For example, using single-nucleus isolation and
312 micromanipulation assays, we previously demonstrated that nuclei with reduced
313 heterochromatin levels are softer and succumb to nuclear blebbing, while nuclei with more
314 heterochromatin levels are stiffer and resist blebbing.[2] This chromatin histone-modification-
315 based nuclear rigidity could be related to the differential transcriptional responsiveness (i.e.,
316 transcriptional plasticity) previously observed in low- versus high-chromatin packing areas upon
317 exposure to external stressors.[48] In many cases, nuclear blebbing is a marker of cell death
318 (i.e., apoptosis) and is often observed during normal developmental processes or in response to
319 various extracellular stressors. The transformation of domains within blebs upon either B-type
320 lamin or heterochromatin enzyme disruption could potentially accelerate these processes by
321 increasing DNA damage or cytoskeletal reorganization. Alternatively, bleb formation could be a
322 necessary event to maintain the stability of the remaining chromatin domains to ensure their
323 continued optimal function by maintaining the optimal conditions for remaining domains to
324 function.

325
326 Although loss of B-type lamins and inhibition of heterochromatin enzymes both induced nuclear
327 morphological changes and increased FMM within nuclear blebs, it is important to consider that
328 these perturbations may not always reflect the same changes in cell phenotype. While B-type
329 lamins are required for proper spatial positioning of heterochromatin and gene-specific loci[8,
330 32, 33], B-type lamin loss and heterochromatin disruption may impact different cellular
331 mechanisms that give rise to these morphological changes. For example, in previous work, we
332 found that decreasing heterochromatin promoted decreased nuclear rigidity and increased
333 nuclear blebbing without necessarily altering lamins.[2] Conversely, removal of B-type lamins
334 resulted in both a reduction of heterochromatin and increased nuclear blebbing.[8, 32, 33]
335 Therefore, while lamins and heterochromatin interact, depletion of either could have differential
336 effects on chromatin organization. In this work, we also found that HDAC or EZH2 inhibition
337 promoted more nuclear deformations in comparison to auxin treatment to remove B-type lamins.
338 As combined treatment of either auxin and TSA or auxin and GSK343 did not result in a more
339 significant increase in these deformations in comparison to TSA or GSK343 alone, our results

340 support previous findings that conclude disruption of chromatin alone is sufficient to cause
341 nuclear blebbing[2]. However, the distortions in the nucleus caused in part by the breakdown of
342 connections between chromatin and the nuclear lamina may be intensified by pressure
343 gradients resulting from external influences.[49]

344
345 These external factors, such as confinement imposed by the actin cytoskeleton or the
346 surrounding environment, could further contribute to the increased deformation of the nucleus.
347 Additionally, processes such as HDACi or HMTi could act by expanding the volume of
348 heterochromatin centers or destabilizing packing domains altogether. In theory, as weak,
349 unstable packing domain (i.e., nascent domain) cores expand in size, one possible
350 consequence could be increased variations in temporally active processes, such as gene
351 transcription, resulting in amplified chromatin motion. Consequently, modifications to higher-
352 order chromatin assemblies could promote bleb formation by degrading packing domains and/
353 or altering chromatin-based nuclear mechanics. However, further assessment is needed to
354 confirm this theoretical interplay between packing domain formation, nuclear mechanics, and
355 transcription.

356
357 The complexity of interactions within the genome results in varying chromatin dynamics at
358 different length scales. Intrinsic characteristics of chromatin, which involve the dynamic
359 rearrangement of histones, interactions among chromosome segments, chromatin remodelers,
360 replication proteins, and transcriptional regulators are required for proper spatiotemporal
361 genome organization. Other than Dual-PWS, several techniques have been utilized to
362 investigate the contributions of chromatin dynamics to this organization. For example, a
363 combination of photoactivated localization microscopy (PALM) and tracking of single
364 nucleosomes was recently applied to assess nucleosome-nucleosome interactions and cohesin-
365 RAD21 in domain formation and dynamics.[50] In line with our results, TSA treatment increased
366 chromatin dynamics. Recently, proximity ligation-based chromatin assembly assays have been
367 applied to investigate the kinetics of nuclear lamina binding to newly replicated DNA in mouse
368 embryonic fibroblasts.[51] Finally, computational models have been applied to probe the time
369 evolution of the chromatin over the G1 phase of the interphase in *Drosophilla* that successfully
370 predict dynamic positioning of all LADs at the nuclear envelope.[52] While Chromatin Scanning
371 Transmission Electron Microscopy (ChromSTEM) does not have live-cell imaging capabilities to
372 resolve chromatin mobility[29], future work may involve this high-resolution imaging technique to

373 investigate how the shift in chromatin dynamics seen here could be related to shifts in chromatin
374 density, volume, and shape.

375

376 **CONCLUSION**

377 The formation of nuclear blebs is believed to be associated with aberrant gene expression in
378 pathological conditions; nevertheless, our understanding of chromatin structure within blebs and
379 the mechanisms resulting in their formation remain poorly understood. The biophysical
380 characteristics of cell nuclei, including their mechanical properties and architecture, play a
381 crucial role in shaping cell phenotype, shape, and function. Our research demonstrates that the
382 transformation of chromatin nanoscopic packing domains may contribute to bleb formation given
383 the structures seen within nuclear blebs on live-cell nanoscopic imaging and super resolution
384 microscopy. This indicates that histone modifications converge in altering chromatin packing
385 domains with the resulting change in structure influencing nuclear mechanics and morphology.
386 As blebs are associated with increased DNA damage, it highlights the need for further
387 investigation into how the change in chromatin structure (both nucleosome modifications and
388 higher-order domains) contribute to transformation of chromatin function within bleb
389 compartments. Future work further investigating blebs can help us understand what happens to
390 gene-transcription within these deformations and how the reintegration of these components of
391 the genome happen during mitosis. Finally, future work to decouple how additional bleb-
392 promoting mechanisms (compression, contraction, translocation) simultaneously at different
393 length scales to organize the genome remains open for further investigation.

394

395

396 **MATERIALS AND METHODS**

397 **HCT116 Cell Culture**

398 HCT116^{LMN(B1&B2)-AID} cells and U2OS cells were grown in McCoy's 5A Modified Medium (#16600-
399 082, Thermo Fisher Scientific, Waltham, MA) supplemented with 10% FBS (#16000-044,
400 Thermo Fisher Scientific, Waltham, MA) and penicillin-streptomycin (100 µg/ml; #15140-122,
401 Thermo Fisher Scientific, Waltham, MA). To create these cells, HCT116 cells (ATCC, #CCL-
402 247) were tagged with the AID system as previously described.[32, 33] All cells were cultured
403 under recommended conditions at 37°C and 5% CO₂. All cells in this study were maintained
404 between passage 5 and 20. Cells were allowed at least 24 h to re-adhere and recover from
405 trypsin-induced detachment. All imaging was performed when the surface confluence of the dish

406 was between 40–70%. All cells were tested for mycoplasma contamination (ATCC, #30-1012K)
407 before starting perturbation experiments, and they have given negative results.

408

409 **Auxin Treatment**

410 HCT116^{LMN(B1&B2)-AID} cells were plated at 50,000 cells per well of a 6-well plate (Cellvis, P12-
411 1.5H-N). To induce expression of OsTIR1, 2 µg/ml of doxycycline (Fisher Scientific, #10592-13-
412 9) was added to cells 24 hours prior to auxin treatment. 1000 µM Indole-3-acetic acid sodium
413 salt (IAA, Sigma Aldrich, #6505-45-9) was solubilized in RNase-free water (Fisher Scientific,
414 #10-977-015) before each treatment as a fresh solution and added to HCT116^{LMN(B1&B2)-AID} cells.

415

416 **GSK343 Treatment**

417 HCT116^{LMN(B1&B2)-AID} cells were plated at 50,000 cells per well of a 6-well plate (Cellvis, P12-
418 1.5H-N). Cells were given at least 24 hours to re-adhere before treatment. GSK343 (Millipore
419 Sigma, #SML0766) was dissolved in DMSO to create a 10 mM stock solution. This was further
420 diluted in complete cell media to a final treatment concentration of 10 µM.

421

422 **Trichostatin A (TSA) Treatment**

423 HCT116^{LMN(B1&B2)-AID} cells were plated at 50,000 cells per well of a 6-well plate (Cellvis, P12-
424 1.5H-N). Cells were given at least 24 hours to re-adhere before treatment. TSA (Millipore
425 Sigma, #T1952) was diluted in complete cell medium and added to cells at a final treatment
426 concentration of 300 nM.

427

428 **Immunofluorescence Sample Preparation**

429 HCT116^{LMN(B1&B2)-AID} cells at a low passage (<P10) were plated at 100,000 cells per well of a 6-
430 well glass-bottom plate (Cellvis, #P06-1.5H-N). Following auxin treatment, cells were washed
431 twice with 1x Phosphate Buffered Saline (PBS) (Gibco, #10010031). Cells were fixed with 4%
432 paraformaldehyde (PFA) (Electron Microscopy Sciences, #15710) for 10 minutes at room
433 temperature, followed by washing with PBS 3 times for 5 minutes each. Cells were
434 permeabilized using 0.2% TritonX-100 (10%) (Sigma-Aldrich, #93443) in 1x PBS, followed by
435 another wash with 1x PBS for 3 times for 5 minutes each. Cells were blocked using 3% BSA
436 (Sigma-Aldrich, #A7906) in PBST (Tween-20 in 1x PBS) (Sigma-Aldrich, #P9416) at room
437 temperature. The following primary antibodies were added overnight at 4°C: anti-H3K27ac
438 (Abcam, #ab177178, dilution 1:7000) and anti-H3K27me3 (Abcam, #ab6002, dilution 1:200).
439 Cells were washed with 1x PBS 3 times for 5 minutes each. The following secondary antibodies

440 were added for 1 hour at room temperature: Goat anti-Rabbit IgG (H+L) Alexa Fluor 568
441 (Abcam, #ab175471, dilution 1:1000) and Goat anti-Mouse IgG (H+L) Highly Cross-Adsorbed
442 Secondary Antibody, Alexa Fluor Plus 647 (Thermo Fisher Scientific, #A32728, dilution 1:200).
443 Cells were washed with 1x PBS 3 times for 5 minutes each. Finally, cells were stained with
444 DAPI (Thermo Fisher Scientific, #62248, diluted to 0.5 $\mu\text{g}/\text{mL}$ in 1x PBS) for 10 minutes at room
445 temperature. Prior to imaging, cells were washed with 1x PBS twice for 5 minutes each.

446

447 **Immunofluorescence Imaging**

448 Live and fixed cells were imaged using the Nikon SoRa Spinning Disk confocal microscope
449 equipped with a Hamamatsu ORCA-Fusion Digital CMOS camera. Live cells were imaged
450 under physiological conditions (37°C and 5% CO_2) using a stage top incubator (Tokai Hit).
451 Images were collected using a 60x/ 1.42 NA oil-immersion objective mounted with a 2.8x
452 magnifier. mClover was excited with a 488 nm laser, Alexa Fluor 647 was excited with a 640 nm
453 laser, and DAPI was excited with a 405 nm laser. Imaging data were acquired by Nikon
454 acquisition software.

455

456 **Dual-PWS Imaging**

457 For live-cell measurements, cells were imaged and maintained under physiological conditions
458 (5% CO_2 and 37°C) using a stage-top incubator (In Vivo Scientific, Salem, SC; Stage Top
459 Systems). Live-cell PWS measurements were obtained using a commercial inverted microscope
460 (Leica, DMIRB) using a Hamamatsu Image-EM charge-coupled device (CCD) camera (C9100-
461 13) coupled to a liquid crystal tunable filter (LCTF, CRi VariSpec) to acquire monochromatic,
462 spectrally resolved images ranging from 500-700 nm at 2-nm intervals as previously
463 described.[38-40] Broadband illumination was provided by a broad-spectrum white light LED
464 source (Xcite-120 LED, Excelitas). The system is equipped with a long pass filter (Semrock
465 BLP01-405R-25) and a 63x oil immersion objective (Leica HCX PL APO). All cells were given at
466 least 24 hours to re-adhere before treatment (for treated cells) and imaging. Briefly, PWS
467 measures the spectral interference signal resulting from internal light scattering originating from
468 nuclear chromatin. This is related to variations in the refractive index (RI) distribution and is
469 captured by the microscope by calculating the standard deviation of the spectral interference at
470 each pixel (Σ). Chromatin packing scaling D was then calculated using maps of Σ . Although it is
471 a diffraction-limited imaging technique, PWS can measure chromatin packing behaviors
472 because the RI of chromatin is proportional to the local density of macromolecules (e.g., DNA,
473 RNA, proteins). PWS senses the complex inhomogeneous RI distribution of chromatins with

474 length scale sensitivity around 20 – 200 nm, and associated it with fractal coefficient, as
475 previously described.[30, 39, 41, 48] PWS measurements were normalized by the reflectance of
476 the glass medium interface (i.e., to an independent reference measurement acquired in a region
477 lacking cells on the dish). This allows acquisition of the interference signal that is directly related
478 to RI fluctuations within the cell. Changes in D resulting from each condition are quantified by
479 averaging cells, taken across 3 technical replicates. Average D was calculated by first
480 averaging D values from PWS measurements within each cell nucleus and then averaging
481 these measurements over the entire cell population for each treatment condition.

482

483 **Dynamic PWS Measurements**

484 Temporal PWS data was acquired as previously described.[32, 39] Briefly, dynamics
485 measurements (Σ_t^2 , fractional moving mass (m_f), and diffusion) are collected by acquiring
486 multiple backscattered wide-field images at a single wavelength (550 nm) over time
487 (acquisition time), to produce a three-dimensional image cube, where Σ_t^2 is temporal
488 interference and t is time. Diffusion is extracted by calculating the decay rate of the
489 autocorrelation of the temporal interference as previously described.[39] The fractional moving
490 mass is calculated by normalizing the variance of Σ_t^2 at each pixel. Using the equations and
491 parameters supplied and explained in detail in the supplementary information of our recent
492 publication [39], the fractional moving mass is obtained by using the following equation to
493 normalize Σ_t^2 by ρ_0 , the density of a typical macromolecular cluster:

494

$$495 \quad \Sigma_t^2 \left(\frac{\pi \rho_0}{2\Gamma^2 k^3 n_i} \right) \left(\frac{NA_i}{NA_c} \right)^2 \left(\frac{n_1}{n_m - n_1} \right)^2 = \rho_0 V_{cm} \varphi = m_c \varphi = m_f \quad (1).$$

496

497 With this normalization, Σ_t^2 is equivalent to m_f , which measures the mass moving within the
498 sample. This value is calculated from the product of the mass of the typical moving cluster (m_c)
499 and the volume fraction of mobile mass (φ). m_c is obtained by $m_c = V_{cm} \rho_0$, where V_{cm} is the
500 volume of the typical moving macromolecular cluster. To calculate this normalization, we
501 approximate $n_m = 1.43$ as the refractive index (RI) of a nucleosome, $n_1 = 1.37$ as the RI of a
502 nucleus, $n_i = 1.518$ as the refractive index of the immersion oil, and $\rho_0 = 0.55 \text{ g cm}^{-3}$ as the dry
503 density of a nucleosome. Additionally, $k = 1.57\text{E}5 \text{ cm}^{-1}$ is the scalar wavenumber of the
504 illumination light, and Γ is a Fresnel intensity coefficient for normal incidence. $NA_c = 1.49$ is the
505 numerical aperture (NA) of collection and $NA_i = 0.52$ is the NA of illumination. As stated
506 previously[39], Σ_t^2 is sensitive to instrument parameters such as the depth of field, substrate

507 refractive index, etc. These dependencies are removed through normalization with the proper
508 pre-factor calculated above for obtaining biological measurements. It should also be noted that
509 backscattered intensity is prone to errors along the transverse direction[39]. Due to these
510 variations, these parameters are more accurate when calculating the expected value over each
511 pixel.

512

513 Chromatin volume concentration is calculated by Fresnel reflection coefficient. Recall that the
514 reflectance at a RI mismatch interface:

515
$$R_s = \left| \frac{n_1 \cos \theta_i - n_2 \cos \theta_t}{n_1 \cos \theta_i + n_2 \cos \theta_t} \right|^2 = \left| \frac{n_1 \cos \theta_i - n_2 \sqrt{1 - \left(\frac{n_1}{n_2} \sin \theta_i\right)^2}}{n_1 \cos \theta_i + n_2 \sqrt{1 - \left(\frac{n_1}{n_2} \sin \theta_i\right)^2}} \right|^2 \quad (2).$$

516
$$R_p = \left| \frac{n_1 \cos \theta_t - n_2 \cos \theta_i}{n_1 \cos \theta_t + n_2 \cos \theta_i} \right|^2 = \left| \frac{n_1 \sqrt{1 - \left(\frac{n_1}{n_2} \sin \theta_i\right)^2} - n_2 \cos \theta_i}{n_1 \sqrt{1 - \left(\frac{n_1}{n_2} \sin \theta_i\right)^2} + n_2 \cos \theta_i} \right|^2 \quad (3).$$

517

518 Although the chromatin is inhomogeneous and not infinitely large, the correlation between
519 chromatin average RI and reflection coefficients still holds as confirmed by Finite Difference
520 Time Domain (FDTD) simulations (**Fig. S3**). Briefly, we used home-built FDTD software to
521 simulate the entire PWS imaging system, from incident to light-matter interaction and then
522 collection.[53] Light beams representing the characteristics of experimental NA_i are first
523 introduced to the simulation space. The simulation space contains a layer of glass and random
524 media that represents chromatin average RI and packing behavior. The EM wave after light-
525 matter interaction is then collected with the same NA_c and far field PWS image is analyzed the
526 same way in experiments. We did a series of simulations with different average RI and
527 measured the mean reflection coefficients. We have fitted:

528
$$\frac{R}{R_0} = 0.36\phi^2 - 1.1\phi + 1.0 \quad (4)$$

529

530 where ϕ is chromatin volume concentration, related to RI through Gladstone-Dale equation [48]:

531

532
$$n_{nucleus} = 1.3446 + 0.0882\phi \quad (5).$$

533

534 **SMLM Sample Preparation and Imaging**

535 Primary antibody rabbit anti-H3K9me3 (Abcam, #ab176916, dilution 1:2000) was aliquoted and
536 stored at -80°C . The secondary antibody goat anti-rabbit AF647 (Thermo Fisher Scientific, #A-

537 21245, dilution 1:1000) was stored at 4°C. The cells were plated on No. 1 borosilicate bottom
538 eight-well Lab-Tek Chambered cover glass with at a seeding density of 1.25×10^4 . After 48
539 hours, the cells were fixed in 3% paraformaldehyde in PBS for 10 minutes, and then
540 subsequently washed with PBS once for five minutes. Thereafter the samples were quenched
541 with freshly prepared 0.1% sodium borohydride in PBS for 7 minutes and rinsed with PBS three
542 times at room temperature. The fixed samples were permeabilized with a blocking buffer (3%
543 bovine serum albumin (BSA), 0.5% Triton X-100 in PBS) for 20 minutes and then incubated with
544 rabbit anti-H3K9me3 in blocking buffer for 1-2 hours at room temperature and rinsed with a
545 washing buffer (0.2% BSA, 0.1% Triton X-100 in PBS) three times. The fixed samples were
546 further incubated with the corresponding goat secondary antibody–dye conjugates, anti-rabbit
547 AF647, for 40 minutes, washed thoroughly with PBS three times at room temperature and
548 stored at 4°C. Imaging of samples was performed on a STORM optical setup built on the
549 commercially available Nikon Ti2 equipped with a Photometric 95B sCMOS camera and a 1.49
550 NA 100X oil immersion objective lens. Samples were illuminated with the MPB Communications
551 2RU-VFL-P-2000-647-B1R 647 nm 200 mW laser. Image acquisition was performed at 20-30
552 ms exposure for 10-15k frames.

553

554 **Data and Image Analysis**

555 We used GraphPad Prism 10.1.1 for making all plots. For immunofluorescence imaging,
556 maximum intensity projection of Z-series images was performed using FIJI.[54] To quantify
557 nuclear deformation frequency, we considered blebs to be herniations that were still connected
558 to the nuclear body. We considered ruptures to be cells that were no longer intact, and we
559 considered micronuclei to be herniations that were no longer connected to the nuclear body and
560 of similar sizes to nuclear blebs. For each field of view, the number of nuclei and the number of
561 each nuclear deformation type was manually counted using FIJI. We then determined the
562 percentages of total cells within each tested condition that displayed each nuclear deformation
563 type.

564

565 **Super-resolution Data Analysis:**

566 We used the Thunder-STORM FIJI Plug-in [55] to apply Maximum Likelihood Estimation fitting of
567 a gaussian point spread function to our image stack. Localization datasets were then put into
568 our Python script that utilized DBSCAN (epsilon=50, min_pts=3) to cluster our localized
569 heterochromatic events. Heterochromatin domain size was estimated by fitting a polygon to the
570 peripheral cluster points using the *scipy* Convex Hull method. Outlier clusters smaller than twice

571 the mean uncertainty of our localization (~ 25 nm) or larger than 800 nm were removed from the
572 analysis. Results displayed are concatenations of identified heterochromatic domains across all
573 cells in that condition.

574

575 **Statistical Analysis and Quantification**

576 Statistical analysis was performed using GraphPad Prism 10.1.1 and Microsoft Excel. Pairwise
577 comparisons were calculated on datasets consisting of, at a minimum, biologically independent
578 duplicate samples using a two-tailed unpaired t test or Mann-Whitney test. The type of statistical
579 test is specified in each case. Experimental data are presented either the mean \pm SEM or mean
580 \pm SD, as stated in figure legends. A *P* value of < 0.05 was considered significant. Statistical
581 significance levels are denoted as follows: n.s. = not significant; **P* <0.05 ; ***P* <0.01 ; ****P* <0.001 ;
582 *****P* <0.0001 . Sample numbers (# of nuclei, *n*), the number of replicates (*N*), and the type of
583 statistical test used is indicated in figure legends.

584

585 **ACKNOWLEDGEMENTS**

586 Microscopy was performed at the Biological Imaging Facility at Northwestern University
587 (RRID:SCR_017767), graciously supported by the Chemistry for Life Processes Institute, the
588 NU Office for Research, the Department of Molecular Biosciences and the Rice Foundation.
589 FDTD simulations were performed at Quest, high-performance computing cluster at
590 Northwestern University.

591

592 **COMPETING INTERESTS**

593 The authors declare no competing interests.

594

595 **FUNDING**

596 This work was supported by NSF grants EFMA-1830961 and EFMA-1830969 and NIH grants
597 R01CA228272, U54 CA268084, and U54 CA261694. L.A. was supported by the NIH Training
598 Grant T32AI083216. A.D.S was funded by the National Institutes of Health Pathway to
599 Independence Award (R00GM123195) and the National Institutes of Health Center for 3D
600 Structure and Physics of the Genome 4DN2 grant (1UM1HG011536). Philanthropic support was
601 generously received from Rob and Kristin Goldman, the Christina Carinato Charitable
602 Foundation, Mark E. Holliday and Mrs. Ingeborg Schneider, and Mr. David Sachs.

603

604 **DATA AVAILABILITY**

605 All relevant data can be found within the article and its supplementary information. The cell lines
606 have been authenticated and are available upon request. Further information and requests for
607 resources and reagents should be directed to and will be fulfilled by the lead contact, Vadim
608 Backman (v-backman@northwestern.edu).

609

610 **AUTHORS' CONTRIBUTIONS**

611 E.M.P. and L.A. wrote the paper and performed immunofluorescence and Dual-PWS imaging
612 and analysis. N.A. and L.A. conducted SMLM imaging and analysis. N.A. assisted with
613 representative Dual-PWS images. Y.S. conducted density estimations from Dual-PWS data.
614 R.G. set up the optical system for all super resolution image acquisition. E.M.P, A.S., L.A., and
615 V.B. conceptualized the project and edited the manuscript.

616

617 **DIVERSITY AND INCLUSION STATEMENT**

618 One or more of the authors of this paper self-identifies as an underrepresented minority.

619

620 **REFERENCES**

- 621 1. Stephens AD, Banigan EJ, Adam SA, Goldman RD, Marko JF. Chromatin and lamin A
622 determine two different mechanical response regimes of the cell nucleus. *Mol Biol Cell.*
623 2017;28(14):1984-96. doi: 10.1091/mbc.E16-09-0653.
- 624 2. Stephens AD, Liu PZ, Banigan EJ, Almossalha LM, Backman V, Adam SA, et al. Chromatin
625 histone modifications and rigidity affect nuclear morphology independent of lamins. *Mol*
626 *Biol Cell.* 2018;29(2):220-33. doi: 10.1091/mbc.E17-06-0410.
- 627 3. Currey ML, Kandula V, Biggs R, Marko JF, Stephens AD. A Versatile Micromanipulation
628 Apparatus for Biophysical Assays of the Cell Nucleus. *Cell Mol Bioeng.* 2022;15(4):303-
629 12. doi: 10.1007/s12195-022-00734-y.
- 630 4. Berg IK, Currey ML, Gupta S, Berrada Y, Nguyen BV, Pho M, et al. Transcription inhibition
631 suppresses nuclear blebbing and rupture independently of nuclear rigidity. *Journal of*
632 *Cell Science.* 2023;136(20).
- 633 5. Chiu K, Berrada Y, Eskindir N, Song D, Fong C, Naughton S, et al. CTCF is essential for
634 proper mitotic spindle structure and anaphase segregation. *Chromosome.* 2023.
- 635 6. Funkhouser CM, Sknepnek R, Shimi T, Goldman AE, Goldman RD, Olvera de la Cruz M.
636 Mechanical model of blebbing in nuclear lamin meshworks. *Proc Natl Acad Sci U S A.*
637 2013;110(9):3248-53. doi: 10.1073/pnas.1300215110.
- 638 7. Nmezi B, Xu J, Fu R, Armiger Travis J, Rodriguez-Bey G, Powell Juliana S, et al. Concentric
639 organization of A- and B-type lamins predicts their distinct roles in the spatial
640 organization and stability of the nuclear lamina. *PNAS.* 2019;116(10):4307-15.
- 641 8. Chang L, Li M, Shao S, Li C, Ai S, Xue B, et al. Nuclear peripheral chromatin-lamin B1
642 interaction is required for global integrity of chromatin architecture and dynamics in
643 human cells. *Protein Cell.* 2022;13:258–80.
- 644 9. Burke B, Stewart CL. The nuclear lamins: flexibility in function. *Nature Reviews Molecular*
645 *Cell Biology.* 2013;14:13-24.
- 646 10. Briand N, Collas P. Lamina-associated domains: peripheral matters and internal affairs.
647 *Genome Biology.* 2020;21(85). doi: <https://doi.org/10.1186/s13059-020-02003-5>.

- 648 11. Greil F, Moorman C, van Steensel B. DamID: mapping of in vivo protein-genome interactions
649 using tethered DNA adenine methyltransferase. *Methods Enzymol.* 2006;410:342-59.
650 doi: 10.1016/s0076-6879(06)10016-6.
- 651 12. van Steensel B, Belmont AS. Lamina-Associated Domains: Links with Chromosome
652 Architecture, Heterochromatin, and Gene Repression. *Cell.* 2017;169(5):780-91.
- 653 13. Lochs SJA, Kefalopoulou S, Kind J. Lamina Associated Domains and Gene Regulation in
654 Development and Cancer. *Cells.* 2019;8(3):271.
- 655 14. Kalukula Y, Stephens AD, Lammerding J, Gabriele S. Mechanics and functional
656 consequences of nuclear deformations. *Nature Reviews Molecular Cell Biology.*
657 2022;23:583–602.
- 658 15. Stephens AD, Banigan EJ, Marko JF. Chromatin's physical properties shape the nucleus
659 and its functions. *Curr Opin Cell Biol.* 2019;58:76-84. doi: 10.1016/j.ceb.2019.02.006.
- 660 16. Karoutas A, Akhtar A. Functional mechanisms and abnormalities of the nuclear lamina.
661 *Nature Cell Biology.* 2021;23:116-26.
- 662 17. Samantha B, Kelsey P, Karan S, Emily Marie P, Pedro P, Julianna A, et al. DNA density is a
663 better indicator of a nuclear bleb than lamin B loss. *bioRxiv.* 2024.
- 664 18. Bunner S, Prince K, Srikrishna K, Pujadas EM, Pellegrino P, Aiello J, et al. DNA density is a
665 better indicator of a nuclear bleb than lamin B loss. *bioRxiv.* 2024.
- 666 19. Vahabikashi A, Sivagurunathan S, Nicdao FAS, Han YL, Park CY, Kittisopikul M, et al.
667 Nuclear lamin isoforms differentially contribute to LINC complex-dependent
668 nucleocytoskeletal coupling and whole-cell mechanics. *Proc Natl Acad Sci U S A.*
669 2022;119(17):e2121816119. doi: 10.1073/pnas.2121816119.
- 670 20. Pho M, Berrada Y, Gunda A, Lavallee A, Chiu K, Padam A, et al. Actin contraction controls
671 nuclear blebbing and rupture independent of actin confinement. *Molecular Biology of the*
672 *Cell.* 2024;35(2).
- 673 21. Jung-Garcia Y, Maiques O, Monger J, Rodriguez-Hernandez I, Fanshawe B, Domart MC, et
674 al. LAP1 supports nuclear adaptability during constrained melanoma cell migration and
675 invasion. *Nat Cell Biol.* 2023;25(1):108-19. doi: 10.1038/s41556-022-01042-3.
- 676 22. Mistriotis P, Wisniewski EO, Bera K, Keys J, Li Y, Tuntithavornwat S, et al. Confinement
677 hinders motility by inducing RhoA-mediated nuclear influx, volume expansion, and
678 blebbing. *J Cell Biol.* 2019;218(12):4093-111. doi: 10.1083/jcb.201902057.
- 679 23. Le Berre M, Aubertin J, Piel M. Fine control of nuclear confinement identifies a threshold
680 deformation leading to lamina rupture and induction of specific genes. *Integr Biol*
681 *(Camb).* 2012;4(11):1406-14. doi: 10.1039/c2ib20056b.
- 682 24. Hatch EM, Hetzer MW. Nuclear envelope rupture is induced by actin-based nucleus
683 confinement. *J Cell Biol.* 2016;215(1):27-36. doi: 10.1083/jcb.201603053.
- 684 25. Evangelisti C, Rusciano I, Mongiorgi S, Ramazzotti G, Lattanzi G, Manzoli L, et al. The wide
685 and growing range of lamin B-related diseases: from laminopathies to cancer. *Cellular*
686 *and Molecular Life Sciences.* 2022;79.
- 687 26. Qin L, He T, Chen S, Yang D, Yi W, Cao H, et al. Roles of mechanosensitive channel
688 Piezo1/2 proteins in skeleton and other tissues. *Bone Research.* 2021;9(44).
- 689 27. Dupouy G, Dong Y, Herzog E, Chabouté M-E, Berr A. Nuclear envelope dynamics in
690 connection to chromatin remodeling. *The Plant Journal.* 2023.
- 691 28. Nava MM, Miroshnikova YA, Biggs LC, Whitefield DB, Metge F, Boucas J, et al.
692 Heterochromatin-Driven Nuclear Softening Protects the Genome against Mechanical
693 Stress-Induced Damage. *Cell.* 2020;181(4):800-17.e22. doi: 10.1016/j.cell.2020.03.052.
- 694 29. Li Y, Agrawal V, Virk RKA, Roth E, Li WS, Eshein A, et al. Analysis of three-dimensional
695 chromatin packing domains by chromatin scanning transmission electron microscopy
696 (ChromSTEM). *Scientific Reports.* 2022;12.

- 697 30. Li Y, Eshein A, Virk RKA, Eid A, Wu W, Frederick J, et al. Nanoscale Chromatin Imaging and
698 Analysis (nano-ChIA) platform bridges 4-D chromatin organization with molecular
699 function. *bioRxiv*. 2020. doi: <https://doi.org/10.1101/2020.01.26.920363>.
- 700 31. Szabo Q, Donjon A, Jerković I, Papadopoulos GL, Cheutin T, Bonev B, et al. Regulation of
701 single-cell genome organization into TADs and chromatin nanodomains. *Nat Genet*.
702 2020;52(11):1151-7. doi: 10.1038/s41588-020-00716-8.
- 703 32. Pujadas EM, Wei X, Acosta N, Carter L, Yang J, Almassalha L, et al. Depletion of lamins B1
704 and B2 alters chromatin mobility and induces differential gene expression by a
705 mesoscale-motion dependent mechanism. *BioRxiv*. 2023. doi: <https://doi.org/10.1101/2023.06.26.546573>.
- 706 33. Pujadas Liwag EM, Wei X, Acosta N, Carter LM, Yang J, Almassalha LM, et al. Depletion of
707 lamins B1 and B2 promotes chromatin mobility and induces differential gene expression
708 by a mesoscale-motion-dependent mechanism. *Genome Biology*. 2024;25(77). doi:
709 <https://doi.org/10.1186/s13059-024-03212-y>.
- 710 34. Stephens AD, Liu PZ, Kandula V, Chen H, Almassalha LM, Herman C, et al.
711 Physicochemical mechanotransduction alters nuclear shape and mechanics via
712 heterochromatin formation. *Mol Biol Cell*. 2019;30(17):2320-30. doi: 10.1091/mbc.E19-
713 05-0286.
- 714 35. Yesbolatova A, Natsume T, Hayashi KI, Kanemaki MT. Generation of conditional auxin-
715 inducible degron (AID) cells and tight control of degron-fused proteins using the
716 degradation inhibitor auxinole. *Methods*. 2019;164-165:73-80. doi:
717 10.1016/j.ymeth.2019.04.010.
- 718 36. Vargas JD, Hatch EM, Anderson DJ, Hetzer MW. Transient nuclear envelope rupturing
719 during interphase in human cancer cells. *Nucleus*. 2012;3(1):88-100. doi:
720 10.4161/nucl.18954.
- 721 37. Chen NY, Kim P, Weston TA, Edillo L, Tu Y, Fong LG, et al. Fibroblasts lacking nuclear
722 lamins do not have nuclear blebs or protrusions but nevertheless have frequent nuclear
723 membrane ruptures. *PNAS*. 2018;115(40):10100 - 5.
- 724 38. Almassalha Luay M, Bauer Greta M, Chandler John E, Gladstein S, Cherkezyan L, Stypula-
725 Cyrus Y, et al. Label-free imaging of the native, living cellular nanoarchitecture using
726 partial-wave spectroscopic microscopy. *PNAS*. 2016;113(42):E6372-E81.
- 727 39. Gladstein S, Almassalha LM, Cherkezyan L, Chandler JE, Eshein A, Eid A, et al. Multimodal
728 interference-based imaging of nanoscale structure and macromolecular motion uncovers
729 UV induced cellular paroxysm. *Nature Communications*. 2019;10(1652).
- 730 40. Gladstein S, Stawarz A, Almassalha LM, Cherkezyan L, Chandler JE, Zhou X, et al.
731 Measuring Nanoscale Chromatin Heterogeneity with Partial Wave Spectroscopic
732 Microscopy. *Methods Mol Biol*. 2018;1745:337-60. doi: 10.1007/978-1-4939-7680-5_19.
- 733 41. Eid A, Eshein A, Li Y, Virk R, Van Derway D, Zhang D, et al. Characterizing chromatin
734 packing scaling in whole nuclei using interferometric microscopy. *Optics Letters*.
735 2020;45(17):4810-3.
- 736 42. Hoskins VE, Smith K, Reddy KL. The shifting shape of genomes: dynamics of
737 heterochromatin interactions at the nuclear lamina. *Current Opinion in Genetics &*
738 *Development*. 2021;67:163-73.
- 739 43. Barth R, Bystricky K, Shaban HA. Coupling chromatin structure and dynamics by live super-
740 resolution imaging. *Sci Adv*. 2020;6(27). doi: 10.1126/sciadv.aaz2196.
- 741 44. Miron E, Oldenkamp R, Brown JM, Pinto DMS, Xu CS, Faria AR, et al. Chromatin arranges
742 in chains of mesoscale domains with nanoscale functional topography independent of
743 cohesin. *Sci Adv*. 2020;6(39). doi: 10.1126/sciadv.aba8811.
- 744 45. Lammerding J, Fong LG, Ji JY, Reue K, Stewart CL, Young SG, et al. Lamins A and C but
745 Not Lamin B1 Regulate Nuclear Mechanics. *Journal of Biological Chemistry*.
746 2006;281(31):25768 - 80.
- 747

- 748 46. Bercht Pflieger K, Taimen P, Butin-Israeli V, Shimi T, Langer-Freitag S, Markaki Y, et al.
749 Gene-rich chromosomal regions are preferentially localized in the lamin B deficient
750 nuclear blebs of atypical progeria cells. *Nucleus*. 2015;6(1):66-76. doi:
751 10.1080/19491034.2015.1004256.
- 752 47. Helfand BT, Wang Y, Pflieger K, Shimi T, Taimen P, Shumaker DK. Chromosomal regions
753 associated with prostate cancer risk localize to lamin B-deficient microdomains and
754 exhibit reduced gene transcription. *J Pathol*. 2012;226(5):735-45. doi:
755 10.1002/path.3033.
- 756 48. Virk RKA, Wu W, Almassalha LM, Bauer GM, Li Y, VanDerway D, et al. Disordered
757 chromatin packing regulates phenotypic plasticity. *Sci Adv*. 2020;6(2):eaax6232. doi:
758 10.1126/sciadv.aax6232.
- 759 49. Cao X, Moeendarbary E, Isermann P, Davidson PM, Wang X, Chen MB, et al. A
760 Chemomechanical Model for Nuclear Morphology and Stresses during Cell
761 Transendothelial Migration. *Biophys J*. 2016;111(7):1541-52. doi:
762 10.1016/j.bpj.2016.08.011.
- 763 50. Nozaki T, Imai R, Tanbo M, Nagashima R, Tamura S, Tani T, et al. Dynamic Organization of
764 Chromatin Domains Revealed by Super-Resolution Live-Cell Imaging. *Mol Cell*.
765 2017;67(2):282-93.e7. doi: 10.1016/j.molcel.2017.06.018.
- 766 51. Lovejoy CM, Nagarajan P, Parthun MR. Dynamic Reassociation of the Nuclear Lamina with
767 Newly Replicated DNA. *Research Square*2023.
- 768 52. Tolokh IS, Kinney NA, Sharakhov IV, Onufriev AV. Strong interactions between highly
769 dynamic lamina-associated domains and the nuclear envelope stabilize the 3D
770 architecture of Drosophila interphase chromatin. *Epigenetics & Chromatin*. 2023;16(21).
- 771 53. Çapoğlu IRT, Allen Backman, Vadim. Angora: A free software package for finite-difference
772 time-domain electromagnetic simulation *IEEE Antennas and Propagation*
773 *Magazine*2013. p. 80-93.
- 774 54. Schindelin J, Arganda-Carreras I, Frise E, Kaynig V, Longair M, Pietzsch T, et al. Fiji: an
775 open-source platform for biological-image analysis. *Nat Methods*. 2012;9(7):676-82. doi:
776 10.1038/nmeth.2019.
- 777 55. Ovesný M, Křížek P, Borkovec J, Svindrych Z, Hagen GM. ThunderSTORM: a
778 comprehensive ImageJ plug-in for PALM and STORM data analysis and super-
779 resolution imaging. *Bioinformatics*. 2014;30(16):2389-90. doi:
780 10.1093/bioinformatics/btu202.

781
782

783 MAIN FIGURE TITLES AND LEGENDS

784 **Figure 1. Aberrant nuclear morphology is induced by the loss of B-type lamins or**
785 **heterochromatin.**

786 **(A)** Percentages of nuclear deformations compiled over each field of view for untreated (control)
787 and 24-hour auxin conditions in HCT116^{LMN(B1&B2)-AID} cells. Each dot represents a technical
788 replicate (N = 3; Control n = 1102, Auxin n = 1081). **(B)** Percentages of nuclear deformations
789 compiled over each field of view for DMSO (vehicle control), 24-hour GSK343, and 24-hour TSA
790 treatment conditions. Each dot represents a technical replicate (N = 3; DMSO n = 295, GSK343
791 n = 1096, TSA n = 456). **(C)** Percentages of nuclear deformations compiled over each field of
792 view for DMSO (vehicle control), 24-hour GSK343 with auxin, and 24-hour TSA with auxin

793 treatment conditions in HCT116^{LMN(B1&B2)-AID} cells. Each dot represents a technical replicate (N =
 794 3; DMSO n = 295, GSK343 + Auxin n = 933, TSA + Auxin n = 456). For **(A-C)**, bar plots are
 795 represented as mean \pm SEM. Unpaired two-tailed t-test with Holm-Šídák test for multiple
 796 comparisons applied in **(B-C)**. **(D)** Representative images of H3K27me3 (magenta), H3K27ac
 797 (yellow), Lamin B1/B2-AID (green), DAPI (blue), and merged fluorescence for control, 24-hour
 798 auxin, 24-hour GSK343, 24-hour GSK343 + Auxin, 24-hour TSA, and 24-hour TSA + Auxin
 799 treatment conditions in HCT116^{LMN(B1&B2)-AID} cells. Scale bar = 10 μ m. **(E)** Corrected total cell
 800 fluorescence measurements of H3K27me3 and **(F)** H3K27ac for control, 24-hour auxin, 24-hour
 801 GSK343, 24-hour GSK343 + Auxin, 24-hour TSA, and 24-hour TSA + Auxin treatment
 802 conditions in HCT116^{LMN(B1&B2)-AID} cells. Each dot represents a cell nucleus. Violin plots show the
 803 median and quartiles. Error bars represent mean \pm SD. One-way ANOVA with Dunnett's test for
 804 multiple comparisons. For **(D-F)**, data are representative of two technical replicates (N = 2, total
 805 n > 150 for each condition). *P \leq 0.05, **P \leq 0.01, ***P \leq 0.001, ****P \leq 0.0001

806

807 **Table 1. Dual-PWS measurements of nuclear blebs.**

Condition	Average <i>D</i> (Mean \pm SEM)	Average FMM (g) (Mean \pm SEM)	Average <i>D_e</i> (μ M ² /s) (Mean \pm SEM)
Control (Untreated)	2.30	1.76*10 ⁻¹⁹	5.09*10 ⁻³
Control (DMSO)	2.22	1.89*10 ⁻¹⁹	5.12*10 ⁻³
(-) Lamin B1/B2	2.37 (\pm 0.03)	2.26*10 ⁻¹⁹ (\pm	4.35*10 ⁻³ (\pm 0.0003)
(-) EZH2	2.27 (\pm 0.03)	2.16*10 ⁻¹⁹ (\pm 1.53*10 ⁻²⁰)	4.71*10 ⁻³ (\pm 0.0001)
(-) HDACs	2.20 (\pm 0.03)	1.99*10 ⁻¹⁹ (\pm 1.53*10 ⁻²⁰)	4.34*10 ⁻³ (\pm 0.0001)

808

809

810 **Figure 2. Loss of B-type lamins, EZH2i, and HDACi induce a bleb-associated chromatin**
 811 **phenotype.**

812 **(A)** Representative PWS *D* maps and *D* values for the nuclear bodies and nuclear blebs for
 813 control and 24-hour auxin-treatment conditions in HCT116^{LMN(B1&B2)-AID} cells. **(B)** Fractional
 814 moving mass values for nuclear bodies and nuclear blebs for control and 24-hour auxin-
 815 treatment conditions in HCT116^{LMN(B1&B2)-AID} cells. **(C)** Effective diffusion coefficient values for the
 816 nuclear bodies and nuclear blebs for control and 24-hour auxin-treatment conditions in
 817 HCT116^{LMN(B1&B2)-AID} cells. **(D)** Representative PWS *D* maps and *D* values for the nuclear bodies
 818 and nuclear blebs for DMSO (vehicle control), 24-hour GSK343, and 24-hour TSA-treatment

819 conditions in HCT116^{LMN(B1&B2)-AID} cells. **(E)** Fractional moving mass values for the nuclear
820 bodies and nuclear blebs for DMSO (vehicle control, 24-hour GSK343, and 24-hour TSA-
821 treatment conditions in HCT116^{LMN(B1&B2)-AID} cells. **(F)** Effective diffusion coefficient values for the
822 nuclear bodies and nuclear blebs for DMSO (vehicle control), 24-hour GSK343, and 24-hour
823 TSA-treatment conditions in HCT116^{LMN(B1&B2)-AID} cells. For **(A-F)**, each dot represents a cell
824 nucleus. (Control n = 2451, Auxin n = 2140, Control Blebs n = 200, Auxin Blebs n = 129, DMSO
825 n = 741, GSK343 n = 790, TSA n = 498, DMSO Blebs n = 564, GSK343 Blebs n = 467, TSA
826 Blebs n = 77). Error bars represent mean \pm SD. Data are compiled from three technical
827 replicates (N = 3). Violin plots show the median and quartiles for the unpaired two-tailed t-test
828 between selected groups. *P \leq 0.05, **P \leq 0.01, ***P \leq 0.001, ****P \leq 0.0001. Scale bars = 5
829 μ m.

830

831 **Figure 3. Chromatin density decreases rapidly in the boundary adjacent to the nuclear**
832 **bleb.**

833 **(A)** Representative mClover signal, fractional moving mass “hot” heat map, and individual
834 frames of the temporal interference signal, inversely proportional to chromatin density over the
835 imaging acquisition time of live HCT116^{LMN(B1&B2)-AID} cells for DMSO (control) and 24-hour TSA
836 treatment from Dual-PWS. Arrows indicate nuclear blebs. Data are representative of three
837 technical replicates (N = 3; DMSO n = 741, TSA n = 498). Fluorescent, fractional moving mass,
838 and individual frame images have the same scaling between treatment conditions. Scale bars =
839 5 μ m. **(B)** Representative chromatin volume concentration (CVC) of a bleb over the acquisition
840 time of dynamic PWS signal. The zig-zag behavior of the temporal signal originated from the
841 moving nature of chromatin and is used to measure FMM. The general trend indicates mass
842 moving out and then moving into the bleb. **(C)** Bleb average CVC for DMSO (control) and 24-
843 hour TSA treatment measured from dynamics PWS signal. Data are the same as of (A). ***P \leq
844 0.001

845

846 **Figure 4. Heterochromatic nanodomains are reorganized during nuclear bleb formation.**

847 **(A)** Representative SMLM images of HCT116^{LMN(B1&B2)-AID} cells with zoomed-in views before and
848 after 24-hour auxin treatment or 24-hour TSA treatment. Yellow: H3K9me3. Data are
849 representative of three technical replicates (N = 3; Control n = 1, Auxin (- Lamin B1/B2) n = 1,
850 TSA (- HDAC) n = 1). Scale bars = 5 μ m for whole nucleus, 1 μ m for inset of whole nucleus
851 (red) and nuclear bleb (blue). **(B)** Representative SMLM images of U2OS cells with zoomed-in
852 views before and 24-hour TSA treatment. Yellow: H3K9me3. Data are representative of three

853 technical replicates (N = 3; Control n = 3, TSA (- HDAC) n = 3). Scale bars = 5 μm for whole
854 nucleus, 1 μm for inset of nuclear bleb (blue). **(C)** Quantification of the number and size of
855 heterochromatin nanodomains in control and TSA treatment conditions for U2OS cells.

856

857 **SUPPLEMENTARY FIGURE TITLES AND LEGENDS**

858 **Figure S1. Nuclear blebbing induces the redistribution and reorganization of packing**
859 **domains.**

860 **(A)** Averages of all three replicates for percentages of nuclear deformations compiled over each
861 field of view for control, 24-hour auxin, DMSO (vehicle control), 24-hour GSK343, 24-hour TSA,
862 24-hour GSK343 with auxin, and 24-hour TSA with auxin treatment conditions. Each dot
863 represents a technical replicate (N = 3; Control n = 1102, Auxin n = 1081, DMSO n = 295,
864 GSK343 n = 1096, TSA n = 456, GSK343 + Auxin n = 933, TSA + Auxin n = 456). **(B)** Averages
865 of all three replicates for *D* values, fractional moving mass, and effective diffusion coefficient for
866 the nuclear bodies and nuclear blebs for control and 24-hour auxin-treatment conditions in
867 HCT116^{LMN(B1&B2)-AID} cells. **(C)** Averages of all three replicates for *D* values, fractional moving
868 mass, and effective diffusion coefficient for DMSO (vehicle control) 24-hour GSK343, and 24-
869 hour TSA-treatment conditions in HCT116^{LMN(B1&B2)-AID} cells. For **(A-C)** means of all replicates
870 are presented above each bar in the plots. Error bars represent mean \pm SEM. For **(B-C)**, Data
871 are compiled from three technical replicates (N = 3; Control n = 2451, Auxin n = 2140, Control
872 Blebs n = 200, Auxin Blebs n = 129, DMSO n = 741, GSK343 n = 790, TSA n = 498, DMSO
873 Blebs n = 564, GSK343 Blebs n = 467, TSA Blebs n = 77).

874

875 **Figure S2. Characterization of heterochromatin nanodomains from SMLM images.**

876 Quantification of the number and size of heterochromatin nanodomains in control, loss of lamin
877 B1/B2, and TSA treatment conditions for HCT116^{LMN(B1&B2)-AID} cells.

878

879 **Figure S3. FDTD simulation confirms the correlation between PWS Intensity with nuclear**
880 **average RI and CVC.**

881 **(A)** Schematic of FDTD simulation setup. Light is illuminated from objective and focused on the
882 cell glass interface. Random media with autocorrelation coefficients representing chromatin are
883 placed into the simulation space. By solving Maxwell equations numerically, the back scattering
884 light intensity field is resolved and used to synthesize simulation PWS images. **(B)** Negative
885 correlation between PWS normalized reflectance and media average RI and ϕ . n = 10 for
886 each condition.

Figure 1

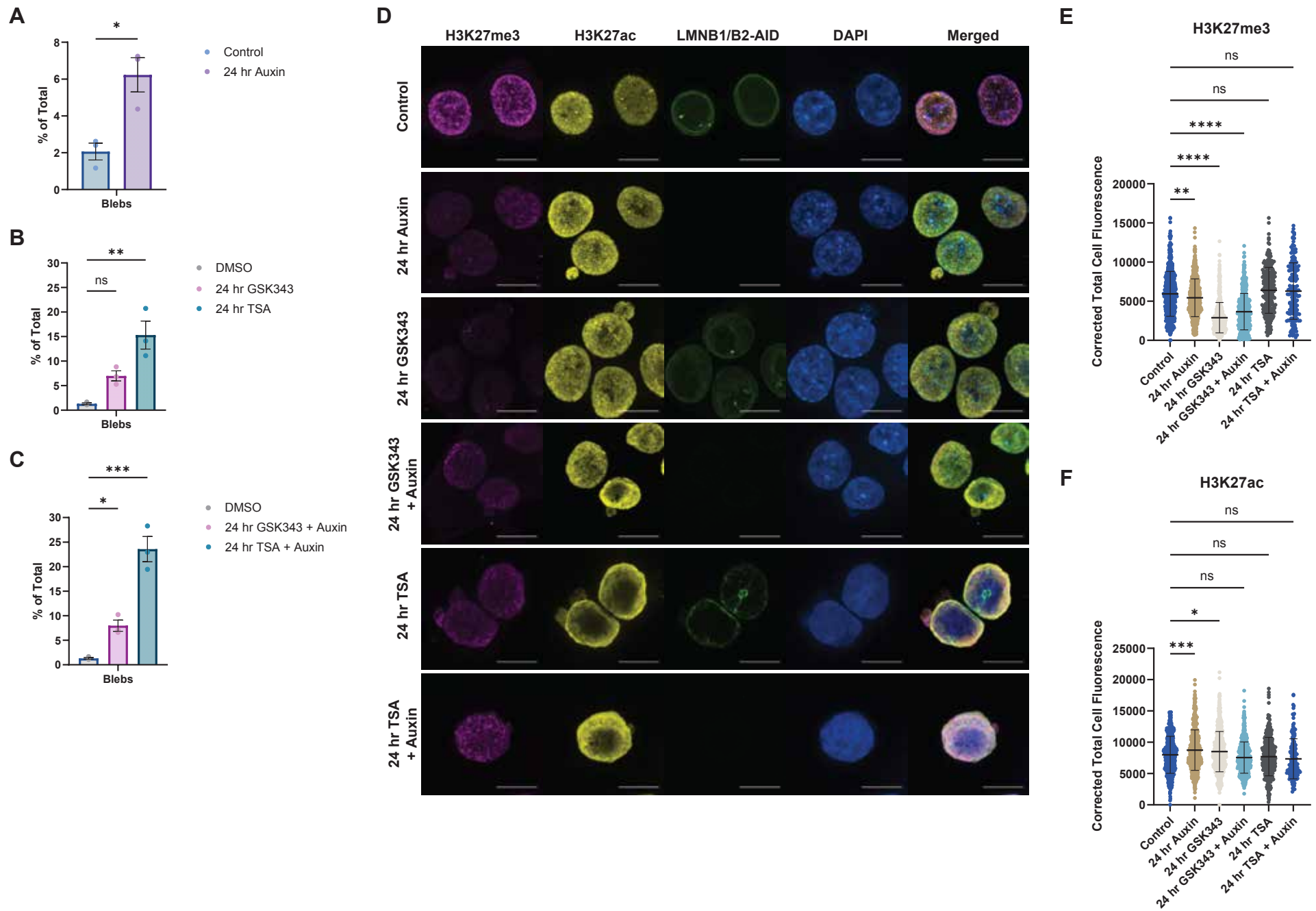
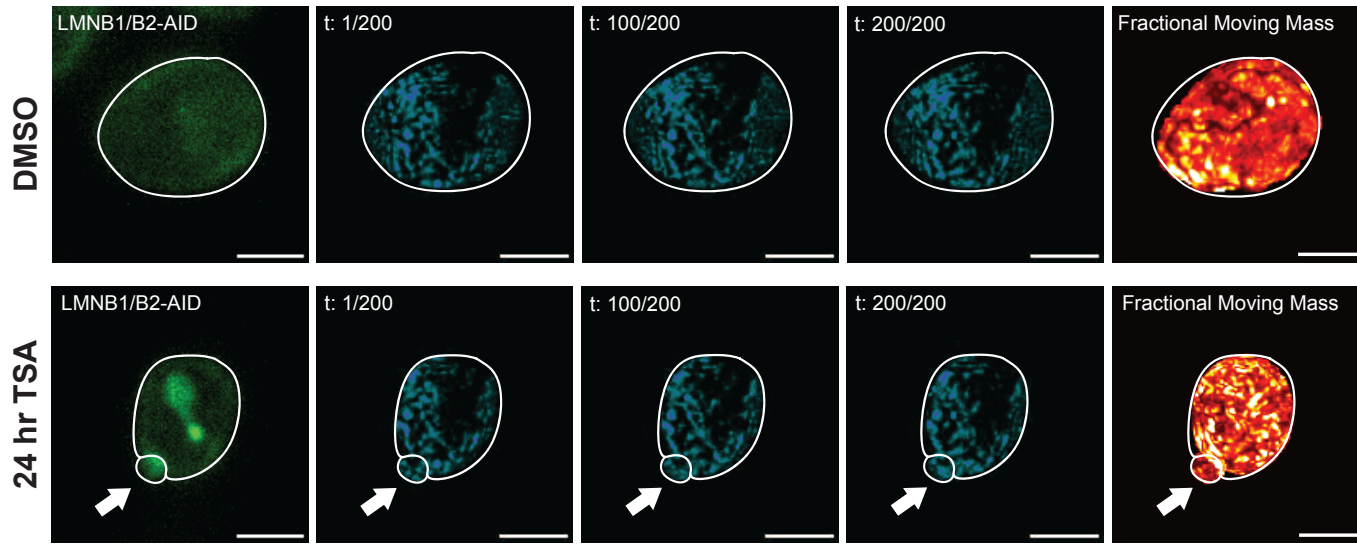
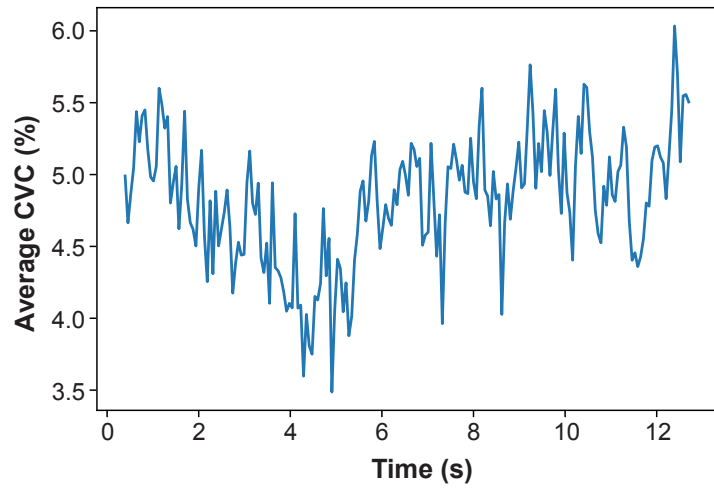


Figure 3

A



B



C

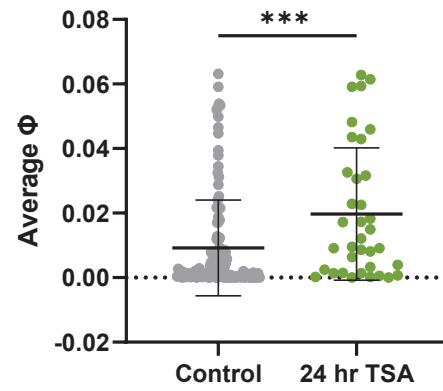
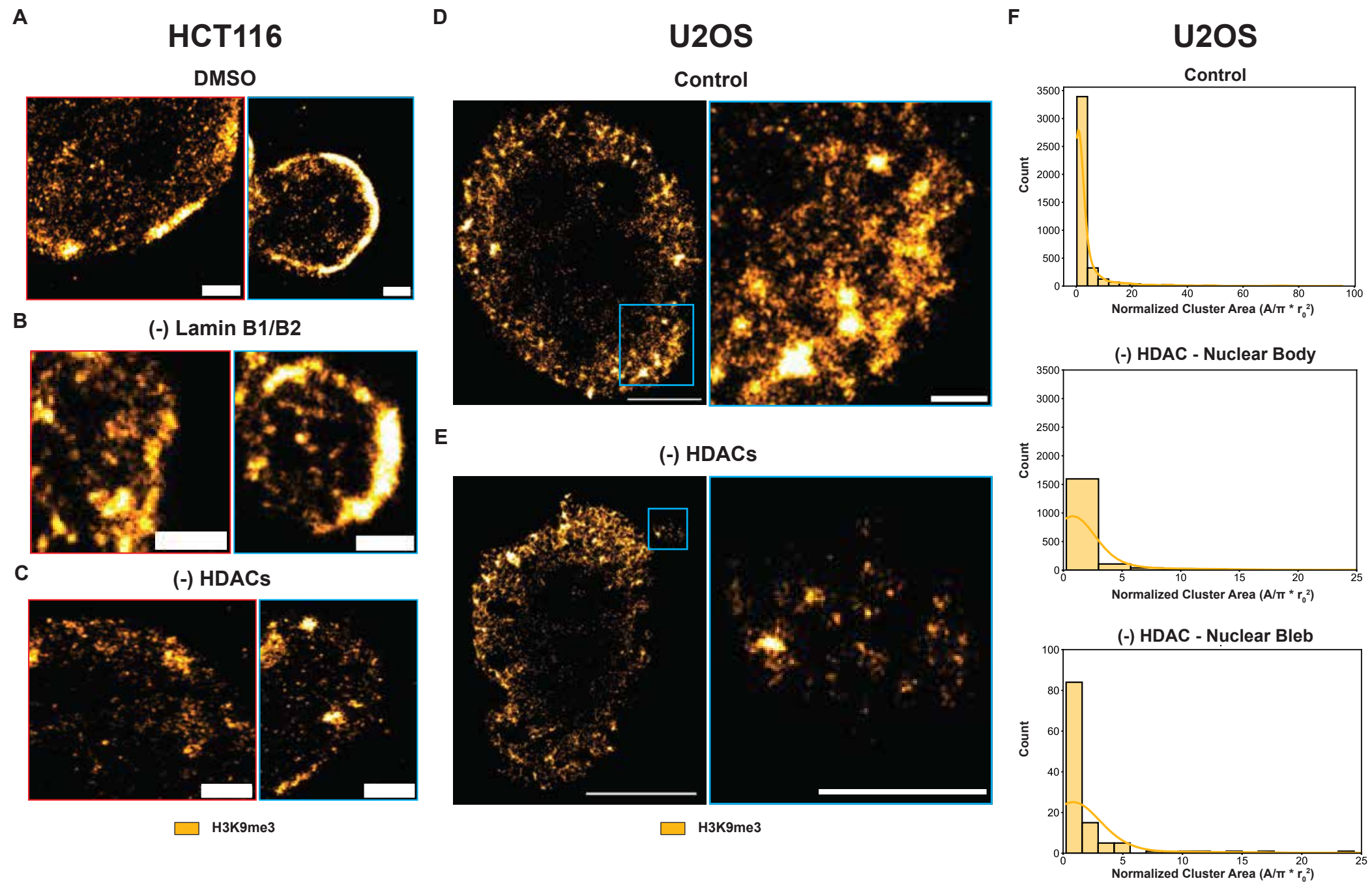
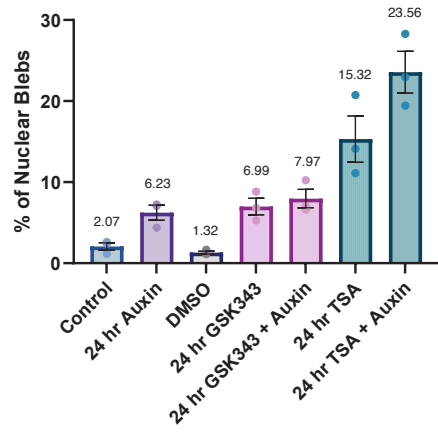


Figure 4

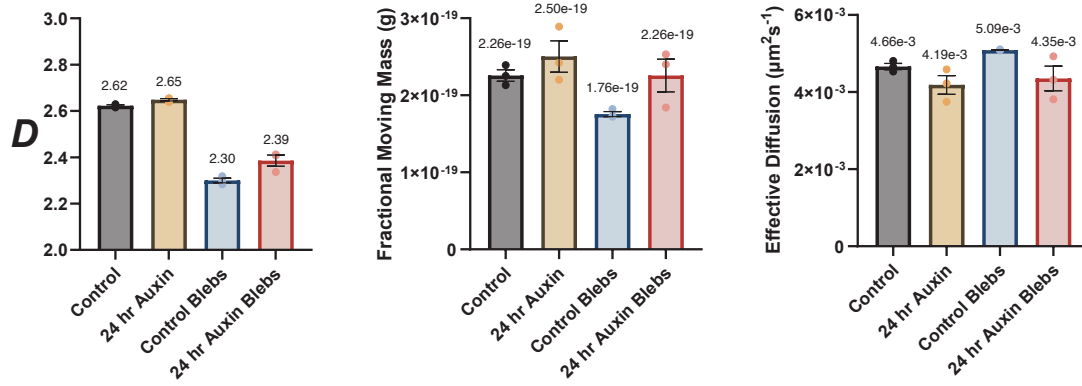


Supplementary Figure 1

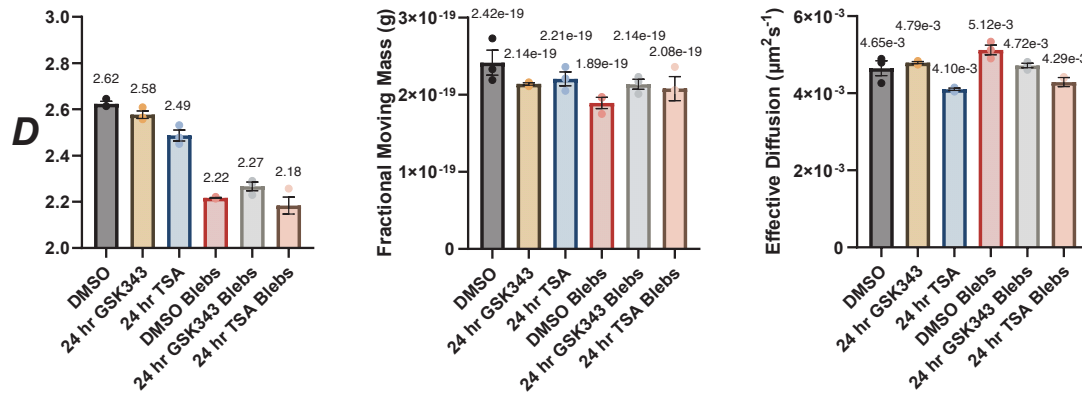
A



B

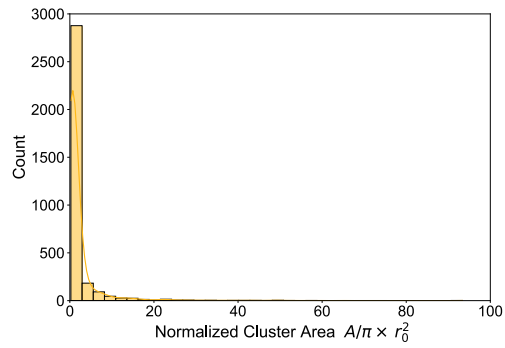


C

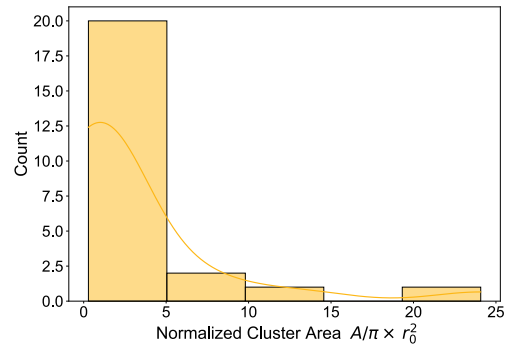


HCT116

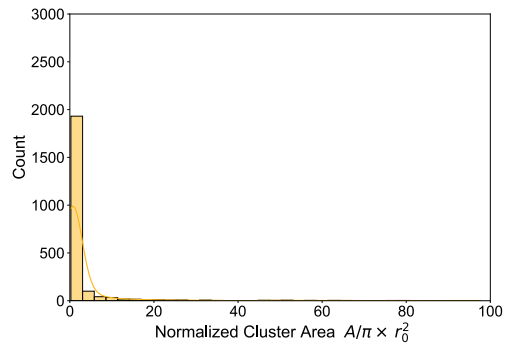
DMSO - Nuclear Body



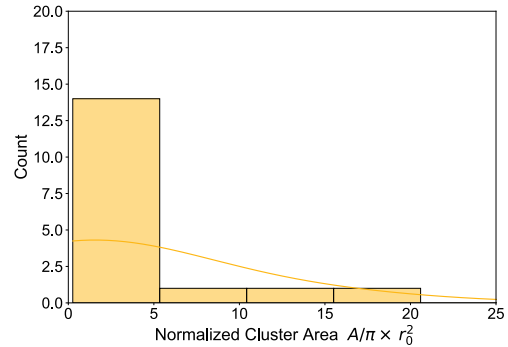
DMSO - Nuclear Bleb



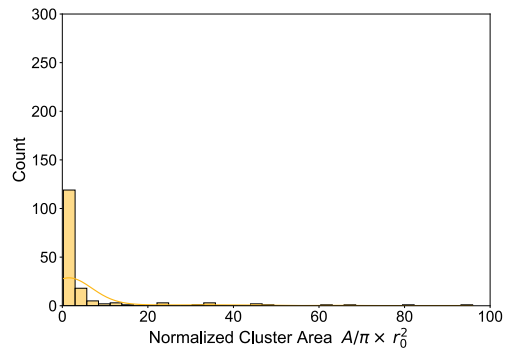
(-) Lamin B1/B2 - Nuclear Body



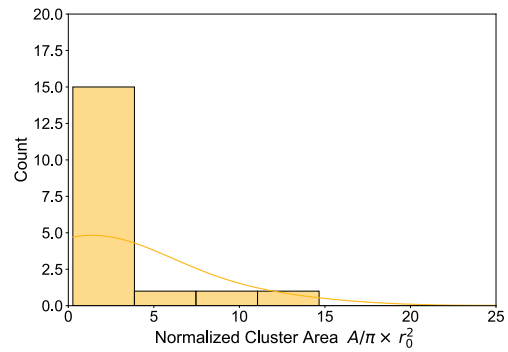
(-) Lamin B1/B2 - Nuclear Bleb



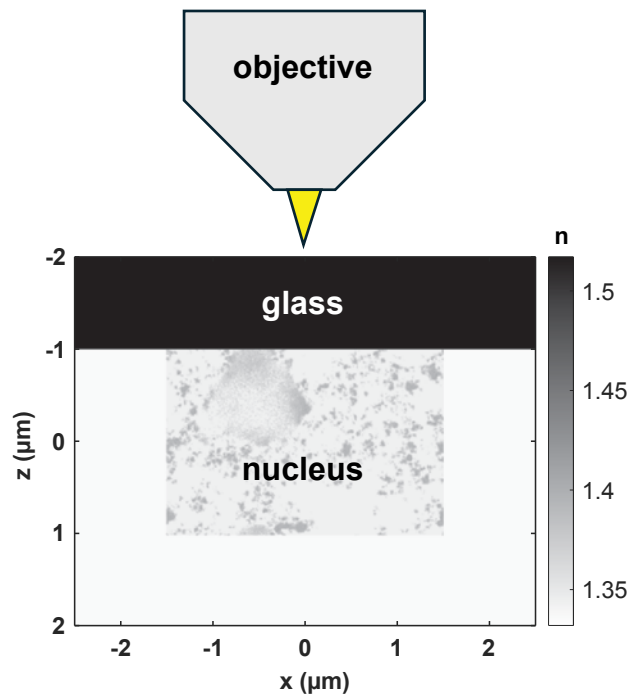
(-) HDAC - Nuclear Body



(-) HDAC - Nuclear Bleb



Supplementary Figure 3

A**B**